Julio A. Z. Ferreira[1] and Jorge G. Zornberg[2]

A Transparent Pullout Testing Device for 3D Evaluation of Soil–Geogrid Interaction

[1] Director, Brazilian Operations, TRI Environmental, São Paulo, SP, Brazil 0001-7563-1307 (Corresponding author), e-mail: jzambrano@utexas.edu, skype: tri-jferreira; Formerly GRA, Department Civil, Architecture and Enviornmental Engineering, The Univ. of Texas at Austin, Austin, TX 78712.

[2] Professor, Department Civil, Architecture and Enviornmental Engineering, The Univ. of Texas at Austin, Austin, TX 78712, e-mail: zornberg@mail.utexas.edu

ABSTRACT

This paper presented a newly developed transparent pullout testing device conceived with the objective of studying the soil–geogrid interaction under small displacements and strains. The bottom plate and the side walls of the pullout box were transparent. The system involved a transparent soil, which was tested as a surrogate for sands in the testing program. The setup led to 3D visualization of the soil–geogrid interaction as it allowed direct visualization of the plan view of the geogrid as well as of the side view of the soil–geogrid interface. Markers embedded in the transparent soil mass allowed tracking of soil particle displacements during the test. The tests were conducted using a polypropylene biaxial geogrid and both transparent soil and a conventional sand. Displacements along the geogrid were obtained continuously using digital image correlation (DIC) techniques in tests with transparent soil, and using tell-tails at five junctions in tests with sand. Comparison of test results with both soils showed that the transparent soil constitutes a good surrogate for sands in pullout studies. The pullout test with transparent soil also indicated that displacements along the geogrid could be properly described using an exponential function. Moreover, exponential fitting to the displacement data led to an exponential distribution of strains along the geogrid during pullout testing. Deflections of transverse ribs were first observed at early stages of the test when only 25 % of the maximum pullout force developed. The observed displacement patterns of the soil markers were useful in defining the zone of influence of the geogrid, which could be successfully quantified using the newly developed testing device. Overall, the new equipment was found to represent an effective tool to better understand the mechanisms involved in soil–geogrid interaction, particularly those that are relevant to quantify the interface stiffness.

Keywords

soil–geogrid interaction, transparent, pullout test, 3D visualization, deflection transverse ribs, geogrid displacement profile, geogrid strain profile

Introduction

Geogrids are extensively used in soil reinforcement applications worldwide. However, design approaches for applications such as the reinforcement of the unbound aggregate in the base course of flexible paved roads still remain highly empirical. This is largely because of the difficulty in quantifying the mechanisms that govern the soil–reinforcement interaction under small displacements. Common approaches used for the design of base course reinforced pavements include the traffic benefit ratio (TBR) and the base course reduction ratio (BCR) (Berg et al. 2000; Perkins and Ismek 1997; Cuelho et al. 2014), two empirical parameters.

TBR is the ratio between the number of cycles until failure of a geosynthetic reinforced cross-section and an unreinforced cross-section. BCR is the percentage of thickness of base course of a reinforced cross-section that can be reduced in relation to an unreinforced base course cross-section to yield similar performance. These empirical approaches are specific to the materials and cross-sections evaluated (Berg et al. 2000; Perkins and Ismek 1997). Consequently, limited information is available on the mechanistic behavior of geogrids for this type of application.

Geogrids have also been used as reinforcement in mechanically stabilized earth (MSE) retaining wall systems. Due to the relatively large reinforcement deformations developed in MSE walls, at least in comparison to base course reinforced pavements, design of geogrid reinforced MSE walls is significantly less empirical than that of reinforced pavements. Nevertheless, available design methods are based on limit equilibrium analyses (Jewell 1992; Berg et al. 2009) or empirical data from working stress conditions (Allen et al. 2003; Bathurst et al. 2008).

Strain data from MSE wall structures have been used to define the shape of the failure surface in limit equilibrium analysis, estimate the tensile load in the reinforcements (e.g., Zornberg et al. 1995; Wei et al. 2002), and to back-calculate geogrid loads to statistically evaluate empirical methods (e.g., Allen et al. 2003; Bathurst et al. 2008). However, in spite of the availability of field data in support of MSE wall design methods, there are still opportunities for better understanding of the mechanistic behavior of the reinforcement and its interaction with surrounding soil.

In summary, limited information is available on the mechanisms of soil–geogrid interaction, especially at the low stress levels in flexible pavements and at the working stress levels in geogrid-reinforced MSE walls. This is due to the difficulty in obtaining quality data on the deformation behavior of the geogrid and the surrounding soil at low stress levels.

A better understanding in support of soil–geogrid interaction mechanisms could lead to improvements in the design for multiple applications involving soil reinforcement, and in particular in the design of reinforced base course pavements. Assessment of the local strains developed in geogrid elements and their interaction with the soil mass are expected to provide a comprehensive understanding of soil–geogrid interaction mechanisms.

Such understanding of the soil–geogrid interaction mechanisms at different stress levels could be achieved by visualization of the deformations that develop in the various geogrid components under confined conditions. Recent improvements in transparent soil technology have made such visualization attainable in addition to the measurement of small strains developed throughout the geogrid and the soil mass.

A newly developed transparent pullout testing device was conceived with the objective of studying the soil–geogrid interaction under small displacements. Specifically, the objectives of this paper are as follows: (i) assess the feasibility of using a transparent soil as a surrogate for sands in pullout tests, (ii) measure the displacement profile, (iii) calculate the strains along geogrids, (iv) obtain data on the deflections along transverse ribs at different loading stages, and (v) analyze the displacement of soil near the soil–geogrid interface.

The transparent pullout test setup developed in the present study was motivated by the need of better understanding soil–geogrid interaction mechanisms in geogrid-reinforced base layer in flexible pavements. Thus, the main focus of this study is to investigate the interaction mechanisms at the local scale of geogrid components.

The paper initially discusses information available in the literature on displacement and strain data along geogrid specimens embedded in soil. Background on the transparent soil and image measurement technologies is also provided. Subsequently, the new transparent pullout testing system is described along with the characterization of the materials used in this research and testing procedures. Next, the data obtained after testing a polypropylene biaxial geogrid are discussed. Finally, the conclusions of this study are presented.

Soil–Geogrid Interaction Mechanisms

Due to its relative simple setup, a common test used to assess soil-reinforced interaction is the pullout test. In this test, a geogrid embedded in compacted soil is pulled out at a constant displacement rate. Typical testing setup involves applying a confining pressure to the soil surface through an air bladder, and an axial load to pull the geogrid out of the box, measured using a load cell at the point of load application.

Pullout tests are mostly applicable to the pullout mode of failure mechanism that develops in MSE walls (Palmeira 2009). Consequently, for its original application, dimensional compatibility between laboratory tests and field conditions was a

concern. Pullout test boundary conditions were extensively investigated (e.g., Farrag et al. 1993; Palmeira and Milligan 1989). Important boundary condition issues that were evaluated include the method of application of the normal load, development of shear stresses against the internal walls of the box, gripping of the geosynthetic specimen, methods of application of the axial load, and characteristics of the front wall of the box.

Pullout tests can also be applicable to the soil–geogrid mechanism developed in reinforced-base course pavements, but not for design purposes. Information on the soil–geogrid interaction at small displacements and strains of the geogrid during these tests may help understand the reinforcement mechanisms in this type of application, besides the different loading conditions between pullout tests and reinforced pavements. In pullout tests, the axial load on the geogrid is applied directly to the reinforcement, which then moves relatively to the soil. In pavements, the geogrid in the base course is loaded indirectly by the displacement of soil particles. Load is applied by the traffic to the surface of the pavement, causing degradation of the base course by the lateral displacement of soil particles. In this case, the main reinforcing mechanism promoted by geogrids is the interlocking of the soil particles through its apertures (Perkins and Ismeik 1997). Thus, the reinforcement is loaded through the soil as opposed to the case of pullout tests.

However, limited information on the behavior of the transverse ribs of the geogrid was obtained from conventional pullout tests in the literature. Measurement of displacements within geogrids in pullout tests was often conducted using mechanical extensometers (or tell-tales), which were attached to the geogrid at its junctions. Moreover, no data on the behavior of the soil adjacent to the geogrid has been obtained from conventional pullout tests.

Despite this limited information, two main mechanisms of shear transfer between geogrid and soil were identified as follows: interface shear and bearing mechanism (Jewell et al. 1984; Farrag et al. 1993). The interface shear develops along the surface of the ribs of the geogrid against soil particles. The bearing

mechanism involves the interlocking of soil particles located within the apertures of the geogrid against the transverse.

Farrag et al. (1993) and Teixeira et al. (2007) performed pullout tests with geogrid specimens with and without transverse ribs. Both studies concluded that the bearing mechanism is the main contributor to the development of pullout forces and is mobilized at relatively large displacement levels.

Dyer (1985) performed pullout tests of metallic grids, with different spacing between transverse members, embedded in a photo-elastic medium. Zones in the medium undergoing higher compressive stresses could be identified in the images. The author showed that the degree of interference between transverse members increases significantly with decreasing spacing between them (**Fig. 1**).

Palmeira (2004) developed a soil–geogrid model based on the progressive mobilization of transverse ribs and the interference between them. The author found good agreement between the pullout force predicted by the model and the pullout test data from Palmeira and Milligan (1989). The results of the model from Palmeira (2004) indicated that mobilization of the second transverse rib closest to front wall is larger than that of the first rib.

Ezzein and Bathurst (2014) investigated the zone of influence of a geogrid and the disturbed zone that developed behind transverse ribs during large scale pullout tests conducted using a biaxial polypropylene geogrid embedded in transparent soil. The authors presented plots with deformation contours of the soil on the longitudinal cross-section of the test. From these plots, it can be observed that the zone of influence of the geogrid extended to approximately 100 mm from the interface.

DISPLACEMENT AND STRAIN IN CONFINED GEOGRIDS

Ezzein and Bathurst (2014) presented displacement profiles at time intervals until rupture along a 2-m long geogrid specimen embedded in transparent soil tested at confining pressures of 10 and 50 kPa. The authors provided continuous displacement measurements along the geogrid length and calculated geogrid lateral strains. Unlike the focus of the transparent pullout box

FIG. 1

Photo-elastic images of pullout tests with metallic grids with different spacing between transverse members: (*a*) large spacing and (*b*) small spacing (modified from Palmeira 2009).
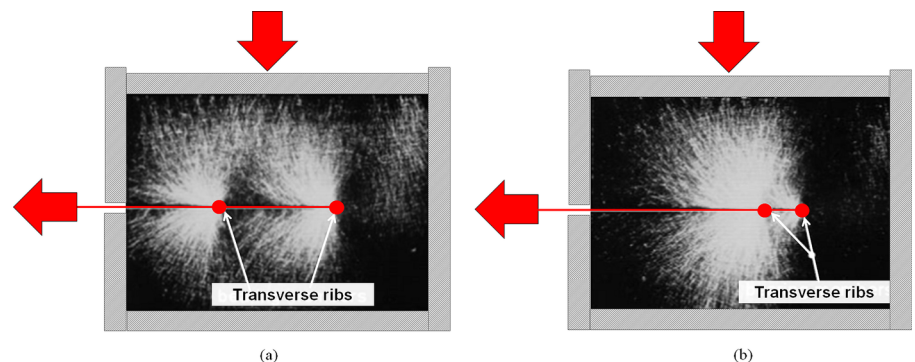
FIG. 2 Strain profile data reported by Chang et al. (1995) and Palmeira (2009). Modified after Chang et al. (1995) and Palmeira (2009).
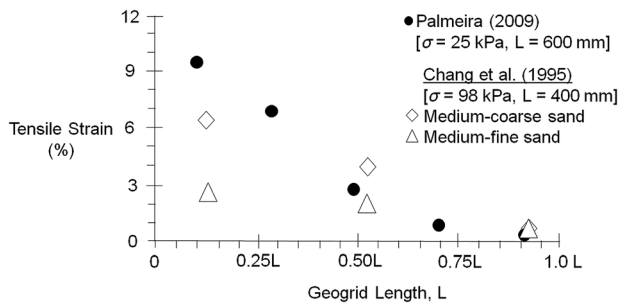
introduced in the present paper, which emphasizes the behavior at the local scale level (i.e., geogrid component behavior), the box developed by Ezzein and Bathurst (2014) focused more specifically on the global scale level (i.e., overall geogrid behavior).

Palmeira (2009) reported pullout test results and finite element method (FEM) simulations conducted by Dias (2003), in which strains along the geogrid specimen calculated from experimental data (**Fig. 2**) were compared with the strains predicted with FEM. Chang et al. (1995) reported limited data of strains measured along the geogrid specimen in large pullout tests. Chang et al. (1995) concluded that the distribution of strains along the geogrid specimen follow a linear pattern (**Fig. 2**).

Calibration of numerical models and determination of continuous strain profiles along the geogrid may become possible with the development of the transparent soil technology. This technology offers the possibility of obtaining quality data that cannot be obtained using conventional pullout tests. The use of transparent soils in pullout tests would allow visualization of the embedded geogrid and continuous measurement of displacements along the longitudinal ribs, the transverse ribs, and in the soil mass surrounding the geogrid.

Transparent Soil

Traditional pullout tests allow displacement monitoring of only a few points along the geogrid specimen. Measurements are conventionally made using wires attached at different junctions of the geogrid specimen, which are in turn connected to displacement sensors. Consequently, the individual contributions of longitudinal and transverse ribs of the geogrid specimen cannot be evaluated with traditional methods. However, recent developments with the transparent soil technology now offer the possibility for such evaluations.

Transparent soils have been used in geotechnical engineering to evaluate a variety of foundation engineering problems

(Wakabayashi 1950; Gill and Lehane 2001; McKelvey et al. 2004; Song et al. 2009). The principle of transparent soils involves submerging a translucent material into a liquid with the same refractive index (RI). This allows making a translucent material become transparent when saturated.

Photo-elastic studies used similar principles as transparent soils. Wakabayashi (1950) used crushed glass and a solution of carbon-disulphide and benzene to conduct photo-elastic studies of stress distribution generated by a loaded footing on the soil surface. Dyer (1985) produced a transparent soil with crushed borosilicate glass and a colorless liquid paraffin to conduct photo-elastic experiments using direct shear and pullout tests. However, photo-elastic studies provide qualitative rather than quantitative data. Moreover, the geotechnical properties of transparent soils obtained from common crushed glass may differ from that of sands (Sadek et al. 2002).

A transparent soil that allowed determination of quantitative data from images was developed by Sadek et al. (2002) using silica gel beads saturated in a blend of white mineral oil and paraffinic solvent. The authors reported geotechnical properties of this transparent soil to be comparable to those of sands after extensive triaxial and direct shear testing. However, two layers of rubber membrane were necessary to perform the triaxial tests because the oil mix was found to attack the membrane, and the authors did not assess the effect of two membranes on the test results.

Moreover, the paraffinic solvent is volatile and classified as hazardous material. The transparency of the soil degraded with time, probably due to the volatility of the solvent and other chemical processes. The silica gel beads are porous, which led to long preparation times as vacuum had to be used to eliminate entrapped air bubbles. Additionally, silica gel beads were found to be highly compressible (Sadek et al. 2002).

Ezzein and Bathurst (2011a) developed a transparent soil for use in a large transparent pullout test apparatus. The transparent soil involved particles of crushed fused quartz, which are non-porous and incompressible. This soil was found to have a geotechnical behavior comparable to that of sands. The matching RI fluid involved non-volatile, non-hazardous, white mineral oils. The transparency of the material was found not to degrade over time.

Ezzein and Bathurst (2011b,2014) used the transparent soil in large scale pullout tests. The bottom plate of the pullout box was transparent and composed of a 25 mm-thick poly(methyl methacrylate) (PMMA) plate. This pullout equipment was larger than traditional pullout equipment that follows the minimum recommendations of the ASTM D6706-01(2013). In traditional tests, the passive end of the geogrid is free to move. Instead, the boundary conditions of the geogrid sample were also different than those of traditional pullout tests, as the geogrid was clamped on the passive end (near the rear wall of the box).

Digital Image Correlation

Digital image correlation (DIC) is a technique used to obtain displacement vectors by comparing consecutive images of the object of interest. The technique has traditionally been used in studies of fluid mechanics in which seeding particles are added to the fluid to calculate particle velocities. These particles have a significant contrast against the fluid; thus acting as tracers. Images obtained at a specific rate during the test are later processed and compared to determine the velocity vectors at each time step.

DIC involves tracking dots with high contrast in the image to define a pattern of different grey shades, or light intensity values. These values are recorded in each pixel to form a 2D array of points in the image of resolution $x \times y$ (e.g., an image with a resolution of 5 megapixels (MP) involves an array of 2452 by 2056 pixels).

The initial step in DIC calculations involves dividing each image into a grid of sub-regions named interrogation areas. The dimensions of the interrogation areas determine the spatial resolution of the measurements (Jensen 2004). Then, two consecutive images can be compared. The pattern of light intensity values for the two images within each interrogation area (IA) is obtained in both images.

A detailed explanation on how the interrogation areas are evaluated using search windows and a cross correlation function is provided by Liu and Iskander (2004). Additionally, details on the processing of the peaks of cross correlation functions are evaluated and on the assignment of displacement vectors are provided by Jensen (2004), Keane and Adrian (1992), Raffel et al. (2007), and White et al. (2003).

Finally, displacements quantified in pixels from the image space are converted into distances (mm) in the object space. This conversion can be done using scale factors defined by obtaining images of an object of known dimensions with the same test setup used for the experiment. More sophisticated models can also be used to take into account significant errors due to radial and tangential distortion created by the curvature and the non-collinearity of the center of multiple lenses of a camera (White et al. 2003).

Distortions increase as the feature of the image is further away from the image center. A common type of lens distortion is the TV distortion, in which a straight line on the edge of an image will be a percentage shorter or larger than its true length (Ren and Wu 2012). A straight line in the center of an image generally has insignificant distortion. **Figure 3** illustrates the case when the TV distortion is negative (barrel distortion).

Other refinements in DIC calculations include the use of overlapped IAs and refinement of the interrogation area in interactive steps using adaptive cross correlation (ACC). Details on the ACC technique are provided by Liu and Iskander (2004).

FIG. 3   Illustration of negative distortion (barrel) in camera lens (adapted from Ren and Wu 2012).
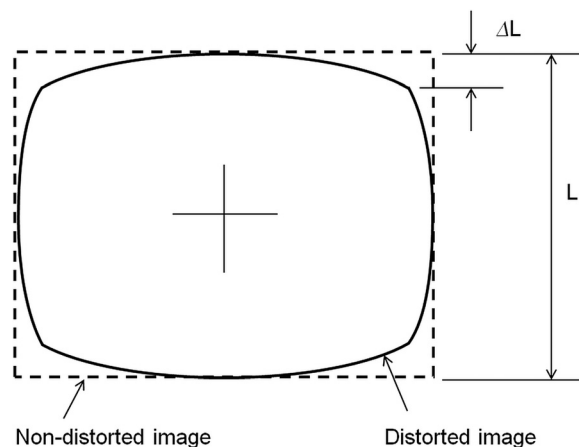
Errors in DIC calculations may arise due to displacement of particles that are perpendicular to the plane of 2D images since displacements in the out-of-plane direction are not captured in the images. To reduce the measurement errors related to out-of-plane motion, the camera needs to be positioned relatively far from the object plane (Dantec Dynamics 2005).

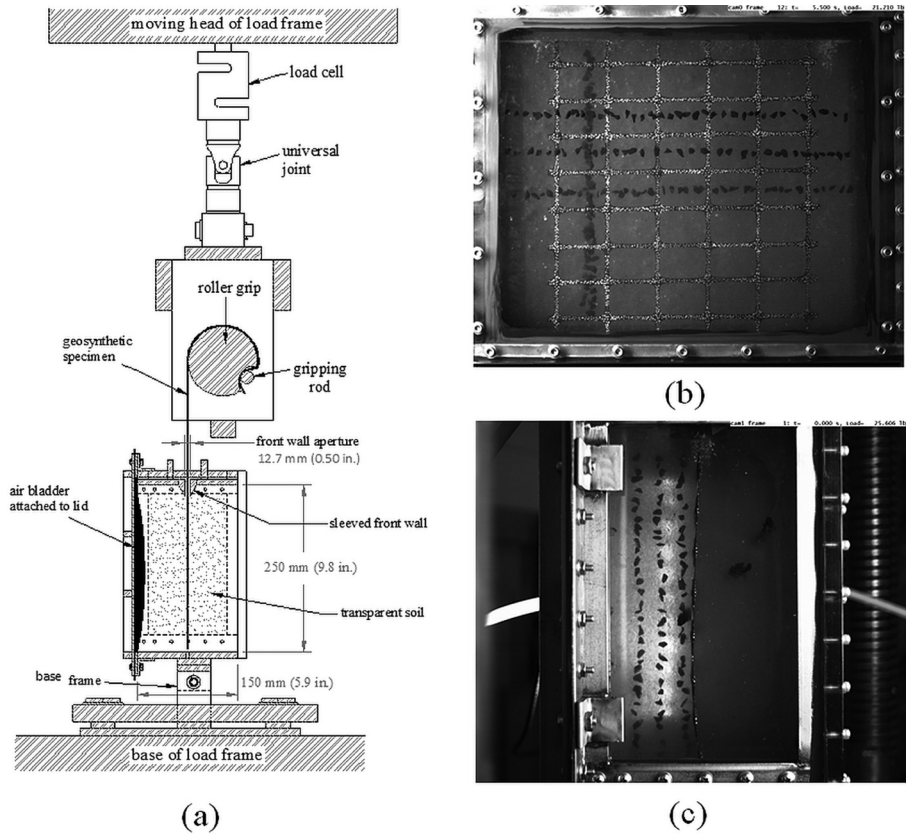## Transparent Pullout Test Device

The transparent pullout test device developed in this research has the basic components of traditional pullout equipment recommended by ASTM D6706. However, the volume of soil used is only 13.1 % of the volume of soil used in a pullout box with the minimum dimensions suggested by ASTM D6706. Additionally, the transparent pullout test device is assembled in the vertical position, making it feasible for testing to be conducted with load frames employed in wide-width tensile strength tests of geosynthetics (ASTM D4595-11 and ASTM D6637-11).

The small pullout testing setup is performed using equipment that is common in laboratories that perform geosynthetic testing. Specifically, only the bottom grip of the wide-width tensile strength test was replaced by the pullout box and its base frame (Zornberg et al. 2013). The implementation of the transparent, small pullout testing setup presented in this paper required an image acquisition system to obtain displacement data.

Figure 4 shows the cross-section of the pullout testing device (**Fig. 4(*a*)**), a typical image of the plan view (**Fig. 4(*b*)**), and an image from the side view (**Fig. 4(*c*)**) of the box. The aperture in the front wall of the pullout box is 12.7 mm, through which the geosynthetic specimen exiting the box is attached to the grip. The internal dimensions of the transparent pullout box are 300 by 250 by 150 mm (width by length by height).

FIG. 4

Transparent pullout test setup: (*a*) cross-section, (*b*) image from the camera on the plan view and (*c*) image from the camera on the side view.

(a)

(b)

(c)

The dimensions of the embedded portion of the geogrid specimen are 216 by 232 mm (width by length).

Figure 5 shows the transparent pullout test setup. Images from the camera on the plan view of the test allow determination of displacements within the geogrid specimen and of soil markers. Images from the camera on the side view allow determination of displacements on the plane perpendicular to the geosynthetic. Measurements from synchronized images obtained from both cameras result in displacement data along three directions, which allows conducting 3D evaluation of soil–geogrid interaction.

Image Data Acquisition System and DIC Software

Displacement data of the entire geogrid specimen were obtained during transparent pullout tests using high definition cameras. The images were acquired using a system that included two 5 MP, 8-bit cameras synchronized with an S-beam load cell. A LabView code was developed for the test device to record the metadata in the right upper corner of the images, displaying the identification of the camera, the time stamp, and the load cell reading at the time that the image was acquired (**Fig. 4(*b*)** and **4(*c*)**).

The cameras were positioned to obtain the plan view of the geogrid as well as the side view of the soil–geogrid interface (Manta G504B and Manta G504C cameras, respectively). Both cameras are manufactured by Allied Vision Technologies, equipped with Sony charge-coupled device (CCD) sensors and capable of acquiring 8-bit images at a maximum rate of 9 frames per second (fps).

FIG. 5   Overview of transparent pullout test setup.
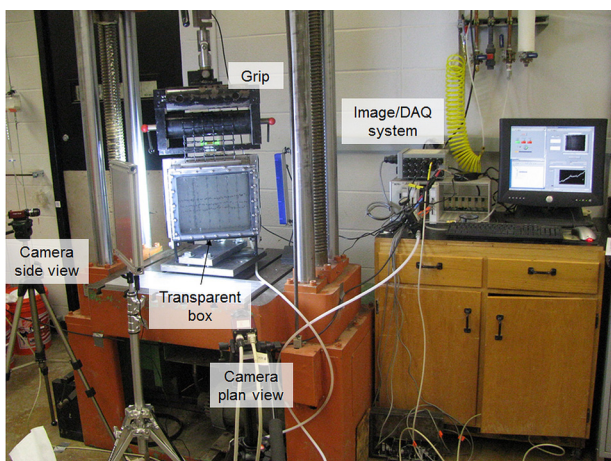
Kowa C-Mount model LM35JCM lenses were used in both cameras. The manufacturer specifications report a TV distortion of only −0.2 % (barrel distortion, see **Fig. 3**) Thus, a straight line at the edge of the image would appear only 0.2 % shorter than its true length with these lenses. In this study, only the displacement measurements of the geogrid and the soil markers from the central portion of the images are used. Thus, measurement errors caused by lens distortion can be assumed to be negligible.

Out-of-plane errors are not a concern for displacements along the geogrid specimen in pullout tests. However, soil markers in the transparent soil may move perpendicular to the camera sensor. To minimize this type of error, the cameras were positioned relatively far from the pullout box as recommended by the supplier of the DIC software (Dantec Dynamics 2005). The images collected during the pullout tests were analyzed using the digital image correlation (DIC) and adaptive cross correlation (ACC) techniques. The software used for these analyses was DynamicStudio v.2.3.0 supplied by Dantec Dynamics.

Soil Characteristics

Two soils were used in this research: Monterey #30 sand and crushed fused quartz (FQ). The particle size distribution curves of the soils are presented in **Fig. 6**. The Monterey #30 sand is a uniformly graded sand that is classified as SP in the unified soil classification system (USCS). This soil is constituted of quartz and smaller amounts of feldspars and other minerals. The particles are rounded to sub-rounded (Li 2005). The Monterey #30 sand was chosen as a baseline for comparison of pullout test results obtained using transparent soil.

The transparent soil used in this research is similar to that used by Ezzein and Bathurst (2011a). This soil is composed of crushed fused quartz particles and two white mineral oils. The fused quartz is a non-porous material with high hardness and

TABLE 1 Properties of the soils.

Property	Monterey Sand	Crushed Fused Quartz
Specific gravity, G_s (ASTM D854)	2.655	2.203
Minimum void ratio, e_{min} (ASTM D4253)	0.52	0.65
Maximum void ratio, e_{max} (ASTM D4254)	0.79	0.83
Uniformity coefficient, C_u	1.5	1.6
Coefficient of gradation, C_c	1.1	1.2
USCS classification	SP	SP

high chemical resistance. It is obtained by melting crystalline silica from quartz sand. Fused quartz is routinely used for manufacturing laboratory glassware, semiconductors, and optical components, among other industries. The crushed fused quartz used in this research has particle sizes in the range of coarse sand with highly sharp particles. The material was supplied by Mintec (Mineral Technology Corporation)[3]. The properties of the soils used in this research are shown in **Table I**.

The fused quartz supplied by Mintec had a maximum diameter, D_{max}, of 6.3 mm with 12 % of the weight of the particles larger than 4.75 mm. The front wall aperture, A, of the transparent pullout box is 12.7 mm, and the thickness, t, of the geogrid ribs used in this research is 1.2 mm. Thus, the ratio $A/(D_{max} + t)$ for the as-received fused quartz was only 1.7. This ratio could lead to undesirable interaction between particles exiting the pullout box and the sleeve at the front wall of the box.

Accordingly, the as-received fused quartz soil was sieved to decrease the maximum particle size diameter to 4.75 mm as shown in **Fig. 6**. Thus, the ratio $A/(D_{max} + t)$ was increased to 2.1. This ratio was found to be adequate to avoid the development of loads unrelated to soil–geogrid interaction.

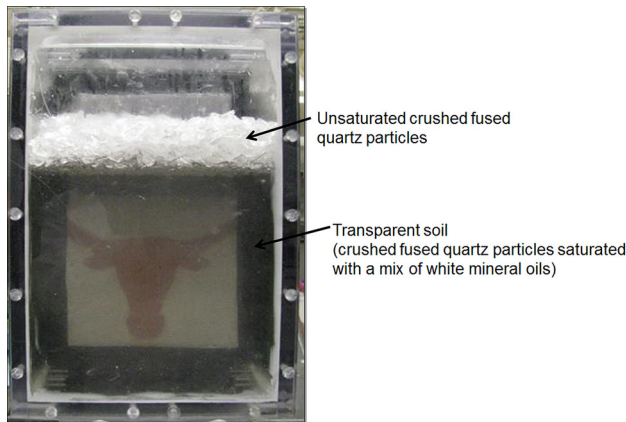## Mineral Oil Mix, Transparent Soil and Soil Markers

The concept of transparent soil involves using a fluid that matches the RI of the granular material so it becomes transparent. The material should be 100 % saturated, as the presence of air bubbles compromises the transparency. The white mineral oils used in this research included Puretol 7 (RI = 1.4637 at 22°C) and Krystol 40 (RI = 1.4458 at 23°C), provided by Petro-Canada. The oil mixture used to match the RI of the fused quartz particles included 69 % of Puretol 7 and 31 % of Krystol 40 by volume at 22°C. This ratio is slightly different from that reported by Ezzein and Bathurst (2011a) due to the different RI of the Krystol 40 oil used in this study. The difference in the reported RI of Puretol 7 is within the range of accuracy of the refractometer. Ezzein and Bathurst (2011a) reported that the viscosity of their mineral oil mix was 10 times higher than

FIG. 6 Particle size distribution curves of the soils used in this research.
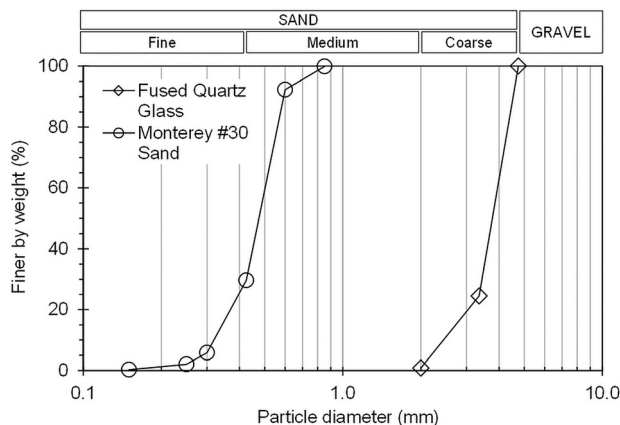
[3]Mintec, PO Box 872, Custer, SD 57730.

FIG. 7   View of transparent soil used in this study.

Unsaturated crushed fused quartz particles

Transparent soil (crushed fused quartz particles saturated with a mix of white mineral oils)

FIG. 8   Failure envelopes from direct shear tests with Monterey sand with water content of 1.5 % and saturated with water.

that of water. Similar viscosity was assumed for the mineral oil mix used in the present study.

The depth of transparent soil that could be observed without loss of transparency was 150 mm looking through a 12.7-mm-thick polycarbonate plate. **Figure 7** shows the transparent soil and unsaturated fused quartz through two 12.7-mm-thick polycarbonates plates and 150 mm of soil.

The soil markers used in this investigation involved fused quartz particles spray-painted with a black color. The use of fused quartz particles as markers minimizes the interference of the markers on the transparent soil behavior, as opposed to when markers of different material than the soil particles are used. Markers with different shape, density, compressibility, etc., than the surrounding soil may influence the behavior of the adjacent soil mass. The markers were placed at different distances from the soil–geogrid interface.

Direct Shear Tests With Monterey #30 Sand

The Monterey #30 sand was tested in a circular shear box with a diameter of 63.5 mm and a height of 31.75 mm, following recommendations by ASTM D3080/D3080M-11. Two series of tests were conducted with a water content of 1.5 % and saturated with water, using normal stresses of 21, 42, and 84 kPa. The average dry unit weight of the sand specimens was 16.3 kN/m^3. The correspondent average relative density (RD) was 70 %.

The failure envelopes for the two series of tests are presented in **Fig. 8**. The regression lines for the envelopes were forced to intercept at zero shear stress to simplify the strength characterization. Friction angles of 39° were obtained for both series of tests. The shear stress versus strain curves are presented in **Fig. 9**. The peaks of shear stress of the tests with saturated water were found to be similar to those of tests with water content of 1.5 % for all normal stresses (**Fig. 9**).
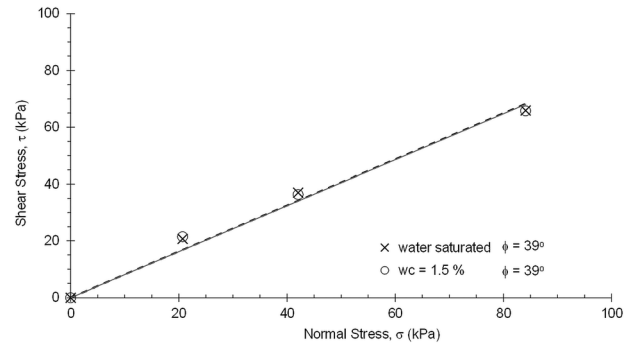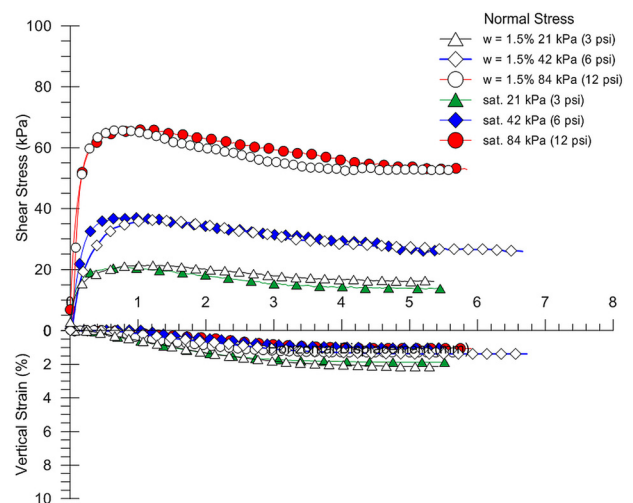
The results show that the Monterey #30 sand dilates during shearing for all normal stresses tested. For both water content conditions, the vertical strain reached constant values after 4 mm of horizontal displacement.
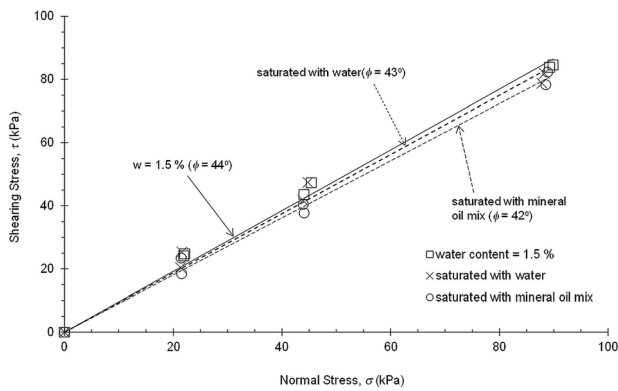
Direct Shear Tests With Crushed Fused Quartz

The particles of crushed fused quartz were sieved to a D_{max} of 4.75 mm to minimize their interaction with the sleeve of the front wall during pullout tests. Accordingly, the same sieved material was used in the direct shear tests. The D_{max} of the sieved fused quartz also conforms to the recommendations of the ASTM D3080, which requires that the width of shear box should exceed 10 D_{max} and that the initial specimen thickness should exceed 6 D_{max}. The crushed fused quartz was tested in a rectangular shear box with dimensions of 76.2 by 76.2 by

FIG. 9   Data of direct shear tests with Monterey sand at a water content of 1.5 % and saturated with water. Positive vertical strains indicate dilation.

30 mm corresponding to width, length, and thickness, respectively.

The direct shear tests with fused quartz included three series of tests: fused quartz with a water content of 1.5 %, saturated with water, and saturated with the mineral oil. The average dry unit weight of the fused quartz specimens in these tests was 13.0 kN/m^3. The average relative density was 77 %, which is similar to that used in the pullout tests.

Tests with fused quartz were conducted with the same initial normal stresses of 21, 42, and 84 kPa used for the tests with sand. In addition, tests were repeated for each confining pressure. The tests saturated with mineral oil mix were prepared using similar procedures to those adopted for the transparent pullout tests. The only difference was that in the series of direct shear tests, the final soil sample height was achieved using three compaction lifts.

The failure envelopes for the three series of tests conducted using fused quartz are presented in **Fig. 10**. As observed in this figure, the friction angles are virtually the same, independent of the pore fluid. The largest difference between friction angles is only 2°, which is within the expected precision of direct shear tests (2°–3°). Therefore, it can be concluded that the peak shear strength is not affected by the pore fluid. Similar results were reported by Ezzein and Bathurst (2011a).

The results of the direct shear tests conducted using fused quartz with a water content of 1.5 % are presented in **Fig. 11**. The results showed that the shear stresses on the fused quartz tend to level to a maximum value with no distinct peak. The Monterey sand shows similar behavior for the normal stresses of 21 and 42 kPa at this same water content. However, for the normal stresses of 84 kPa, the Monterey sand and the fused quartz were observed to behave differently. The Monterey sand showed a smooth peak and a gradual decrease of the shear stress after the peak (**Fig. 9**). The fused quartz tended to a nearly constant value of maximum shear stress for larger deformations (**Fig. 11**).
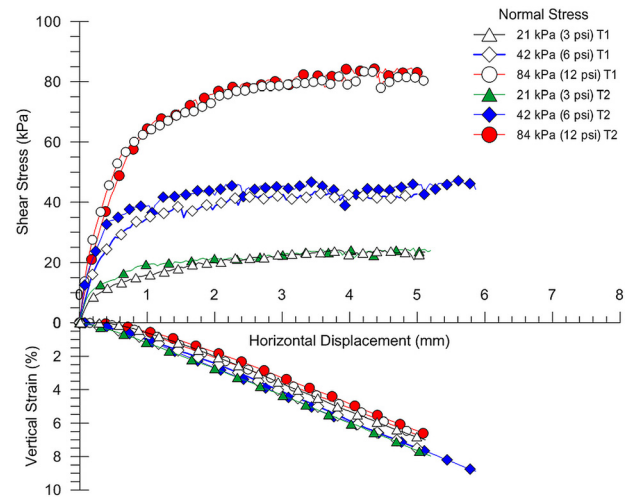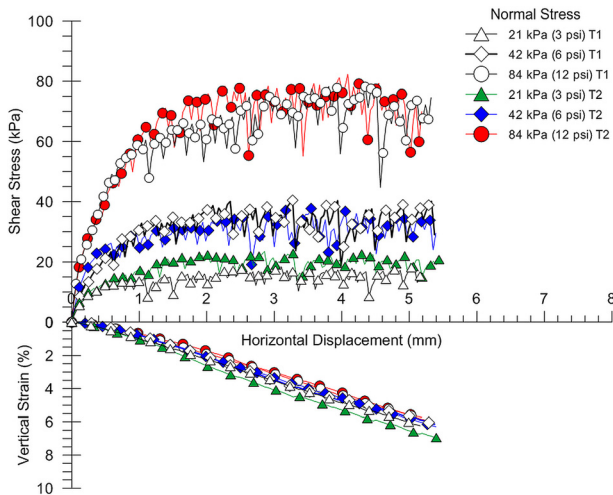
The vertical strain data observed in **Fig. 11** show that the fused quartz dilates almost linearly with increasing displacements in the range of normal stresses and horizontal displacements tested. Unlike the behavior observed in the Monterey sand, no constant maximum vertical strain was reached. This behavior was also observed in the tests with coarse fused quartz reported by Ezzein and Bathurst (2011a).

The shearing behavior of the fused quartz saturated with water was found to be similar to that with a water content of 1.5 %. On the other hand, the overall shearing behavior of the fused quartz saturated with the mineral oil mix (i.e., transparent soil) was comparable but with distinct features. The results of the direct shear tests using fused quartz saturated with mineral oil mix are presented in **Fig. 12.** A slip-stick phenomenon was observed in these tests, in which cycles of shear stress were observed to drop and recover during the test. The load drops increase for increasing normal stresses.

Additionally, the vertical strain results for this series of tests were found to be similar to those observed in the series of tests with water as the pore fluid. The fused quartz saturated with the mineral oil mix was found to also dilate almost linearly with increasing horizontal displacements for the range of normal stresses tested. However, the vertical strains were smaller than those obtained when testing fused quartz saturated with water and with a water content of 1.5 %

A detail discussion of this slip-stick phenomenon is provided later in this paper. The slip-stick phenomenon was also observed by Ezzein and Bathurst (2011a) in direct shear tests and by the present authors during the pullout test with transparent soil. They attributed the occurrence of these cycles to the alignment of particles while shearing along the principal

FIG. 12 Direct shear test data for fused quartz saturated with mineral oil mix. Note: T1 = test 1; T2 = test 2 (repeat of test 1).

Multi-rib tensile tests using geogrid samples in the MD from the same lot used in the present study were conducted by Gupta (2009) following the recommendations by ASTM D6637. The tests were conducted with a grip displacement rate of 10 % per minute, which corresponds to a displacement rate of approximately 25 mm/min. These tests were performed at Texas Research International (TRI). The measured average tensile strength of the geogrid in the MD was 13.8 kN/m with relatively small variation of the results. The average strain of the geogrid at breakage was 16.5 %, with comparatively large variation of the results (Gupta 2009).

stress direction, through which inter-particle forces form chains that are in a fragile equilibrium, constantly collapsing, and realigning.

Geogrid Characterization

The nominal specifications of the geogrid product used in this research, Tensar BX1100, are presented in **Table 2**. The pullout tests used to compare the results with Monterey #30 sand and crushed fused quartz at 1.5 % of water content were conducted using geogrid specimens oriented in the cross-machine direction. The orientation of the geogrid was chosen by the authors to compare to the results reported by Zornberg et al. (2013). However, the pullout test with transparent soil was conducted using geogrid specimens oriented in the machine direction (MD). This was because the spacing between ribs in the MD is larger, resulting in longer transverse ribs, which are expected to result in larger deflections during testing.

Evaluation of Image Acquisition System and DIC Calculations

In order to validate the DIC calculations from the images obtained using the image acquisition system developed in this study, multi-rib tensile tests were conducted using geogrid samples in the MD from the same lot tested by Gupta (2009), in accordance with ASTM D6637.

Five tensile tests were conducted by Gupta (2009), complemented by three additional tests in this study. **Figure 13** shows the results of representative tests from both studies. **Figure 13** shows that there is good agreement between the tests conducted by Gupta (2009) and by the authors with the developed image acquisition system. The average ultimate tensile strength of the geogrid measured was 14.4 kN/m, only 4 % above the 13.8 kN/m obtained by Gupta (2009). The average strain of the geogrid at breakage was 16.4 %, virtually the same 16.5 % obtained by Gupta (2009).

The five tests conducted by Gupta (2009) resulted in coefficients of variation of 0.7 and 15.3 % for the ultimate tensile strength and strain at rupture, respectively. The three tests conducted in the present study resulted in coefficients of variation of 3.1 and 16.0 % for the ultimate tensile strength and strain at rupture, respectively. Thus, the agreement between the

TABLE 2 Nominal specifications of the geogrid used in this research (Tensar Corporation).

Characteristics			Geogrid Orientation	
			MD[a]	CD[b]
Mechanical properties				
	Tensile strength (kN/m) at ASTM D6637	$\varepsilon = 2\%$	4.1	6.6
		$\varepsilon = 5\%$	8.5	13.4
		Ultimate	12.4	19.0
	Junction efficiency (%) GRI-GG2		93	—
	Junction strength (kN/m) calculated from junction efficiency		11.5	—
Geometric properties	Aperture dimensions (mm)		25	33
	Minimum rib thickness (mm)		0.76	0.76
Polymer/aperture geometry/manufacturing process			Polypropylene/rectangle/integrally formed	

[a]MD = machine direction.
[b]CD = cross machine direction.

(a)   (b)

(c)   (d)
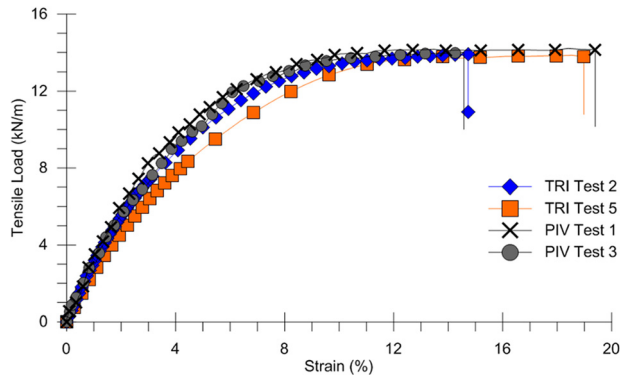
experimental results and the low coefficients of variation validates the DIC calculations adopted in this study.

The DIC software used for displacement measurements from the images is the DynamicStudio v.2.30 supplied by Dantec Dynamics. Before obtaining displacement data, measurements with the DIC software were calibrated using images obtained from the two cameras which were pre-processed and analyzed. The calibration of displacements obtained with DIC calculations was performed with images of 512 by 512 pixels cropped from the transparent pullout test.

This calibration involved two stages. In the first stage, cropped images from the camera on the plan view were used. Vertical displacements (dy) were digitally applied to a reference image by cropping different images using Adobe Photoshop Elements offset by the number of pixels desired for the displacement. Displacements of 1, 2, 4, 8, 16, and 32 pixels were used for the calibration. The reference cropped image and the images with vertical displacements of 8, 16, and 32 pixels are presented in **Fig. 14**.

The images were analyzed using the DIC program with six different configurations for the parameters of the ACC analyses. These parameters included (i) the size of the final IA, (ii) the number of refinement steps, and (iii) the overlap between adjacent interrogation areas. The configuration that provided the best results was with a final IA of 32 by 32 pixels, 3 refinement steps (initial IA of 256 by 256 pixels) and an overlap of 25 %.

With the final configuration, the average error on displacement calculations was only 0.00061 pixel (or 0.003 % of the digitally applied displacement). However, this should not be considered the standard error for all DIC calculations with images from the plan view camera. These errors were evaluated only for applied integer values of displacements.

Sub-pixel displacements result in larger errors because of the need of interpolation of the cross correlation function for resolutions higher than 1 pixel. Raffel et al. (2007) reported that errors on the order of 0.05–0.1 pixel are realistic for
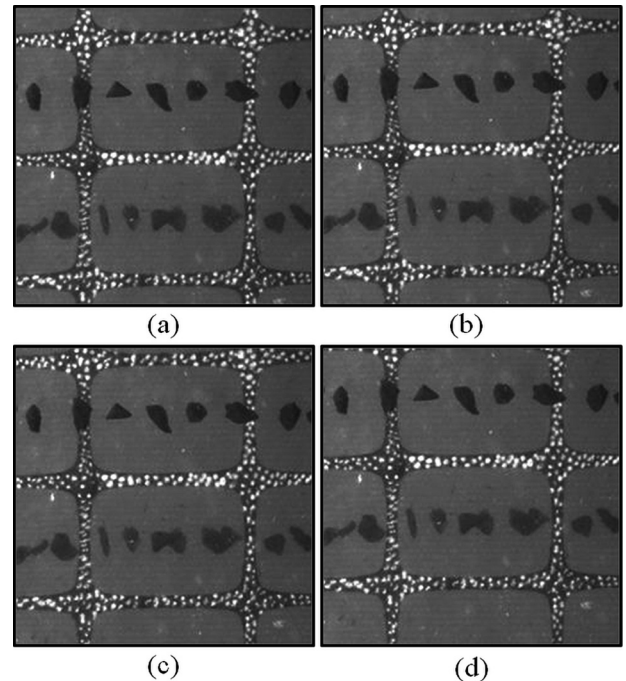
interrogation areas of 32 by 32 pixels from 8-bit digital images. White et al. (2003) reported that errors of approximately 0.005 pixel can be achieved.

Testing Program and Procedures

SCOPE OF THE TESTING PROGRAM

The scope of the testing program discussed in this paper includes four pullout tests (**Table 3**). The first three tests involved a geogrid tested in the cross-machine direction (CD) under a confining pressure of 21 kPa. The soils used were Monterey sand, crushed fused quartz, and crushed fused quartz saturated with the white mineral oil mix (i.e., the transparent soil). This configuration for tests was adopted to allow future comparisons of these results to those reported by Zornberg et al. (2013).

The objective of the tests using the geogrid in the CD was to evaluate the feasibility of using artificial soil composed of fused quartz as a surrogate of sandy. In addition, the influence of the white mineral oil on the results was evaluated by comparing the results of the tests conducted using fused quartz at a water content of 1.5 %.

With the geogrid aligned in the CD, the first rib transverse to the pullout direction is located at the beginning of the front wall sleeves. To minimize the possibility that this first transverse rib pushes soil particles against the sleeves at the front wall

TABLE 3 Testing matrix adopted in this research.

Geogrid		Soil	Confining Pressure
Orientation	Configuration		
CD[a]	1st transverse cut	Monterey sand at wc[d] = 1.5 %	21 kPa (3 psi)
CD	1st transverse cut	Fused quartz at wc = 1.5 %	21 kPa (3 psi)
CD	1st transverse cut	Transparent soil[c]	21 kPa (3 psi)
MD[b]	No modifications (eight transverse ribs)	Transparent soil	35 kPa (5 psi)

[a]CD = Cross-machine direction.
[b]MD = Machine direction.
[c]Transparent soil = fused quartz saturated with the mineral oil mix.
[d]wc = water content.

aperture, this first transverse rib was removed. This was not necessary for the fourth test, which was conducted with the geogrid aligned in the MD, since the location of the first transverse rib was sufficiently distant from the sleeves. Also, the confining pressure adopted in the fourth test was 35 kPa.

TESTING PROCEDURES WITH MONTEREY #30 SAND AND FUSED QUARTZ AT 1.5 % WATER CONTENT

The procedure adopted for the pullout tests with Monterey #30 sand and fused quartz with a target water content of 1.5 % involved initial lining of the internal walls of the box with two layers of polyester film sheet. White lithium grease was used between the wall and the first layer of polyester film sheet and between both layers of polyester film sheet. The layers of polyester film sheet were used to minimize friction between the soils and the box walls.

The compaction of the bottom layer was conducted in four lifts by hand, tampering with a steel rod of 32 mm in diameter. The mass of soil for each lift required for the target dry density was measured prior to placement of the soil into the box. After compaction of each lift, the surface of the soil was scarified before placement of the mass of soil of the next lift.

Following completion of the bottom layer, the geogrid specimen was placed and the wires were attached passing through the aperture of the rear wall of the pullout box. The top layer of soil was then compacted in four lifts using the same procedure. A gap of 5 mm was left between the soil surface and the top of the box. This gap was to accommodate a piece of non-woven geotextile that was placed on the soil surface to protect the air bladder from puncturing. Finally, the lid was secured and the confining pressure was applied to the soil through the air bladder.

Only after application of the confining pressure was the box placed in a vertical position and attached to the base frame on the load frame. The displacement sensors were then aligned to the wires of the tell-tails connected to the geogrid and locked in place in the base frame. Finally, the geogrid was attached to the grip and a pre-load of 0.13 kN was applied. The pullout tests were conducted at a rate of 1.0 mm/min. The test was terminated when a constant, maximum pullout force was reached.

TESTING PROCEDURES WITH TRANSPARENT SOIL

Before compaction of the fused quartz, white dots were painted in a dense mesh on the geogrid specimen to provide the color contrast needed for DIC calculations. The pullout test was prepared with the box initially placed horizontally and with a rubber piece in the front wall aperture to prevent loss of mineral oil. The soil was compacted in eight 19-mm thick compaction lifts. For each lift, the amount of mineral oil mix sufficient to submerge one compaction lift was first poured into the box. Then, the desired mass of fused quartz was pluviated into the box in 3 steps.

A glass pipette was subsequently used to carefully stir the transparent soil, causing air bubbles in the oil mix to rise. The soil was hand tamped with a 32 mm diameter steel rod until reaching the desired final height. Any remaining air bubbles were allowed to rise after tamping. Finally, the surface of the soil was carefully scarified and the volume of oil mix for the next lift was cautiously poured. Additional air bubbles were allowed to rise before pouring the mineral oil mix for the next lift. This process was repeated until reaching the desired soil sample.

It was observed that several fused quartz particles did not become transparent when immersed in the mineral oil mix, having the appearance of a cloud with a dense concentration of white dots. This lack of transparency was caused by small air bubbles entrapped in the interior of the fused quartz particles during production of the material. An optical microscope was used to obtain a detailed image of a particle of fused quartz that had entrapped air bubbles in its interior (**Fig. 15**).

When the compacted transparent soil mass reached the front wall aperture at mid-height of the box, the rubber seal was removed, the leaked oil mix was collected, the geogrid was carefully placed in the box, and the front wall aperture was sealed using modeling clay. The next step involved cautiously replacing the collected oil mix in the box so air bubbles did not develop, and finally completing the compaction of the soil in the box.

FIG. 15   Optical microscopic view of a fused quartz particle with entrapped air bubbles.

After compaction, pieces of a white woven geotextile, non-woven geotextile and polyester film sheet were placed in this order on the soil. The white geotextile was used to create a background contrast with the black geogrid specimen. The non-woven geotextile was used to protect the air bladder against puncture from the angular fused quartz particles. Although the non-woven geotextile became saturated with mineral oil, a piece of polyester film sheet was used to minimize friction between the non-woven geotextile and the air bladder.

The next step involved applying a confining pressure of 7 kPa with compressed air supplied into the air bladder. This initial confinement was to minimize disturbance in the soil–geogrid system when positioning the pullout box vertically.

Next, the modeling clay was removed and the final confining pressure of 35 kPa was applied. Then, the pullout box was placed on the base frame and secured in place.

Subsequently, the geogrid was attached to the grip. The cameras and lighting system were carefully positioned and aligned with the pullout box. The cameras were aligned with the pullout box by using a professional I-beam level, rafter square and chalk reel line. A pre-load of 0.15 kN was applied to the geogrid. Finally, the test was initiated with synchronized images and load cell readings. The displacement rate of the grip was 1.0 mm/min throughout the test.

After the test was finished, the geogrid was disconnected from the grip and the pullout box was put aside on a separate table without changing the position of the cameras. A calibration box was placed on the base frame of the pullout box, and calibration images were obtained with the cameras used during the pullout test. These images were used to relate measurements in the image space (pixels) to measurements in the object space (mm). For the transparent pullout test analyzed in this paper, 1 pixel was equivalent to 0.13835 mm.

The calibration box included a ruler embedded in compacted transparent soil and involved transparent walls of the same characteristics as those in the pullout box. The distance between the box wall and the ruler is the same as the distance between the pullout box wall and the geogrid (**Fig. 16**). Thus, distortions due to the magnification effect caused by refraction of light in the transparent soil mass were taken into account as part of this calibration procedure.

The transparent soil tests conducted under a confining pressure of 21 kPa were terminated after reaching a maximum, constant pullout force. The transparent soil test conducted under a confining pressure of 35 kPa was terminated when reaching tensile failure, since this occurred before a maximum
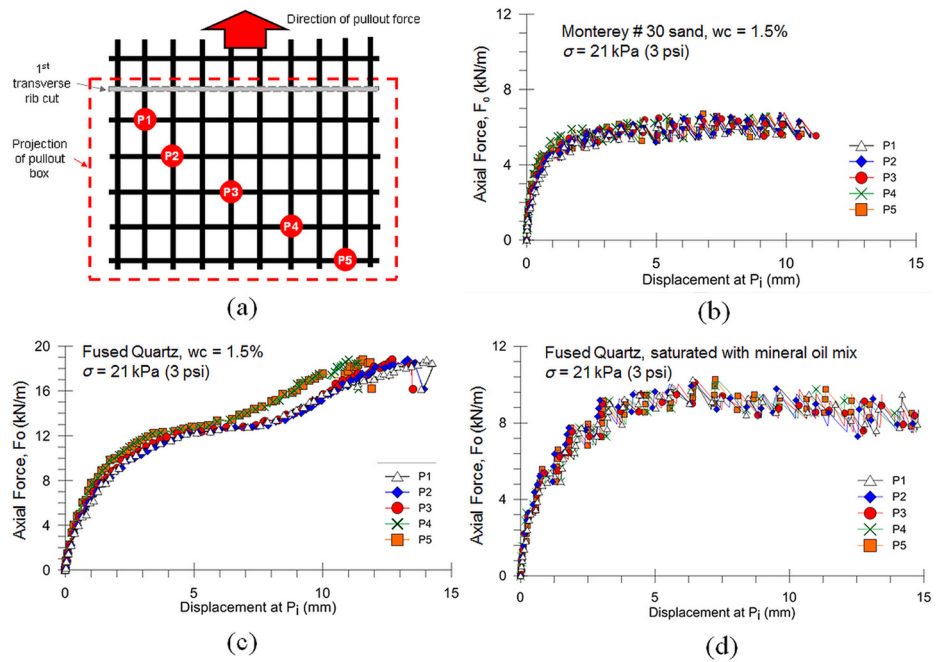
FIG. 16

Calibration box with ruler embedded in transparent soil in similar conditions as the geogrid embedded in transparent soil in pullout tests: (*a*) front view, (*b*) diagonal view, and (*c*) side view.

Same distance between pullout box boundary and geogrid

(a)   (b)   (c)
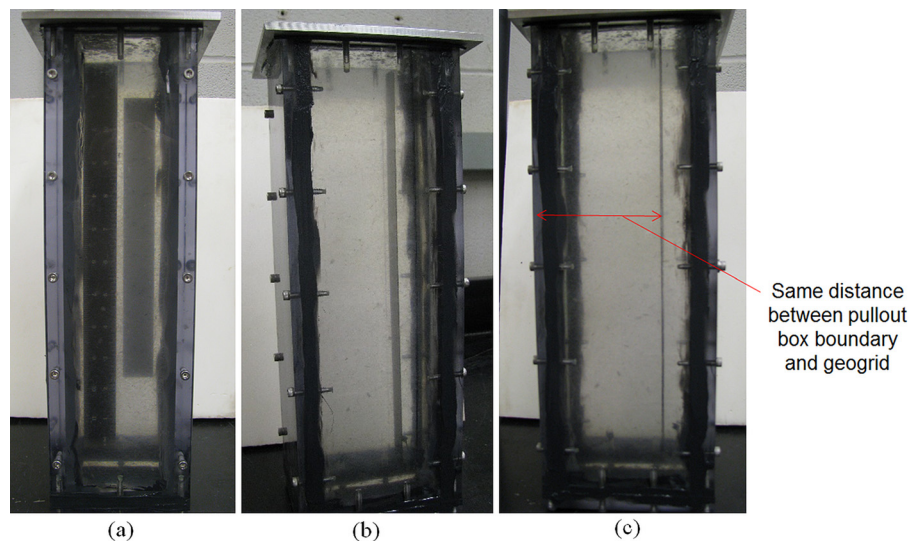
FIG. 17

Results from small pullout tests conducted with the geogrid on the CD and confining pressure of 21 kPa: (*a*) sketch of the location of the LVDT(s) along the geogrid specimens in all tests, (*b*) Monterey #30 Sand and wc ≅ 1.5 %, (*c*) fused quartz with wc = 1.5 % and (*d*) fused quartz saturated with the mineral oil mix (i.e., transparent soil). Note: Pi = point i for LVDT i; F_o = axial force measured by the load cell.

Feasibility of Transparent Soil as a Surrogate for Sands in Pullout Tests

The small pullout test conducted using Monterey #30 sand and geogrid in the CD was prepared with sand at a water content of 1.33 % and dry unit weight of 15.9 kN/m³. This corresponds to a RD of 54 %. A small pullout test was performed with crushed fused quartz compacted at a water content of 1.26 % and dry unit weight of 12.6 kN/m³. This corresponds to a RD of 46 %.

The dry unit weight of the pullout test with transparent soil was 12.7 kN/m³. This corresponds to a RD of 60 %. A lower RD was difficult to achieve because compaction of the fused quartz was facilitated by the presence of the mineral oil mix. The oil was found to lubricate the contact between the particles; thus the mass of fused quartz densified significantly with comparatively low compaction effort.

In these tests, displacements along the geogrid were monitored using tell-tails at five different junctions distributed along the geogrid specimen. The embedded length of the geogrid was 232 mm for all pullout tests. The pullout curves of the tests are presented in **Fig. 17**, where the horizontal axis is the displacement at Point *i* (P_i) along the geogrid (e.g., P1 corresponds to the location of the first linear variable differential transformer (LVDT)). The vertical axis corresponds to the axial force F_o

pullout force was reached. The tensile failure occurred in the unconfined portion of the geogrid specimen between the box and the roller grip.

measured by the load cell. The lowest maximum axial force obtained was 6.8 kN/m with the Monterey #30 sand. This was expected since this is a finer material than the fused quartz.

In the test conducted using fused quartz with water content of 1.5 % (**Fig. 17(c)**), the axial force was found to increase until reaching a constant value of 12.5 kN/m. However, the axial force was found to subsequently increase again until breakage of the geogrid at 19 kN/m. The value of 12.5 kN/m, at which the axial force reached an initial plateau, was considered the maximum axial force of the test. The increase of the axial force beyond this value was attributed to the friction resistance developed by the displaced soil in contact with the surfaces of the sleeve when exiting the box. The crushed fused quartz is highly dilative (**Fig. 11**), so additional friction was created against the surfaces of the sleeve of the box since they restrain the dilation of the soil. Thus, the pullout curve considered for the test with fused quartz with water content of 1.5 % was regarded to reach a maximum value of 12.5 kN/m (**Fig. 17(c)**).

Additionally, in the test with transparent soil (**Fig. 17(d)**), the pullout force reached a constant value. This is because the oil lubricated the contact of the fused quartz along the surfaces of the sleeve when the particles exit the box. As a result, no additional pullout load is generated.

Comparison between the results in **Fig. 17(b)** and **17(c)** reveals that saturation of the particles of fused quartz in mineral oil led to a decrease in the axial force developed throughout the test. The overall trends of the pullout curves shown in **Fig. 17** are consistent with pullout test results reported in the literature (Farrag et al. 1993; Gupta 2009; Palmeira and Milligan 1989;

Ochiai et al. 1996; Teixeira et al. 2007). Thus, it was concluded that the transparent soil with crushed fused quartz saturated in mineral oil can be used as a surrogate for sands in pullout tests.

A slip-stick behavior was observed, which involved cycles of sudden drops in the pullout load, followed by load recovery in the tests conducted using Monterey #30 sand and fused quartz saturated with the mineral oil mix (**Fig. 17(a)** and **Fig. 17(c)**, respectively). At the time of the load drops, the entire geogrid was observed to move at once. The load recovery was observed to occur as relatively small displacements developed. These cycles started when reaching 65 and 30 % of the maximum pullout resistance in the tests conducted using sand and transparent soil, respectively. This phenomenon was not observed in the direct shear tests conducted using Monterey #30 sand, but it was observed in the direct shear tests with transparent soil.

On the other hand, the slip-stick phenomenon was not observed in the test conducted using fused quartz at the water content of 1.5 % (**Fig. 17(b)**). These results suggest that the slip-stick behavior (**Fig. 17(c)**) was caused by the presence of mineral oil on the contact between fused quartz particles. This lubrication was reported to prevent larger chains of particles from forming that would support the load (Ezzein and Bathurst 2011a). As the load increases, the chains of particles slide over each other more easily; thus the slip-stick phenomenon occurred at small pullout loads and displacements.

Nakamura et al. (2003) reported pullout results with similar cycles of drops and recovery of the pullout load in tests conducted using a fine sand and pullout box with dimensions comparable to the one used in the present study. However, the cycles of load drops and recovery in the results of Nakamura et al. (2003) started only after the maximum pullout force was reached. Zornberg et al. (2013) reported similar results for pullout tests conducted using Monterey #30 sand in a small pullout box of the same internal dimensions to the transparent pullout box used in the present study. The only differences between the pullout boxes are that the small pullout box used by Zornberg et al. (2013) does not have a sleeve and the front wall aperture is larger.

Displacement and Strain Profiles of Geogrid Embedded in Transparent Soil

GEOGRID DISPLACEMENT PROFILES: DATA POINTS AND CURVE FITTING MODEL

Displacement profiles at different load levels were obtained using DIC calculations along the geogrid specimen oriented in the MD in the transparent pullout test conducted using 35 kPa of confining pressure. While the complete testing program involved five transparent pullout tests with different geogrid

FIG. 18 Displacement profile of L3 at different load levels of the pullout test conducted with transparent soil and geogrid oriented in the MD confined under 35 kPa. Note: F_o = pullout force measured by the load cell.
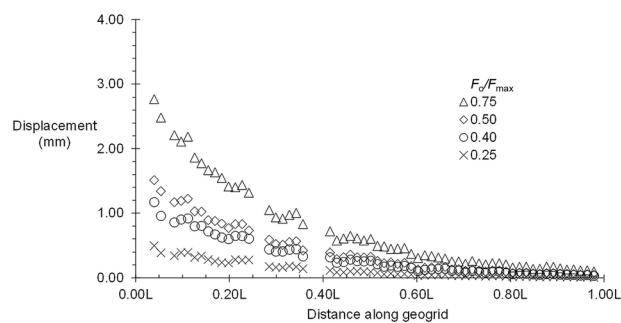
configurations, the scope of the present paper is on the developed test setup and the model adopted to best fit the displacement data.

The displacement data of the tests were found to fit an exponential function well. Fitting a curve to the displacement data allows for the calculation of the strains from the derivative of the fitted curve. This approach was found to be significantly better than calculating strains directly from displacement of two consecutive data points, which was found to introduce significant scatter in the results.

Only the data of the two central longitudinal ribs, namely L3 and L4, were used in the analyses. These ribs are in the central portion of the images, where image distortion is minimal. **Figure 18** presents the displacement profile data from L3. The data from L3 were first used in the data fitting process because these are the best quality data, with more data points in the active portion of the geogrid.

The equation adopted to fit the displacement data of all transparent pullout tests is the following exponential equation:

$$y = \alpha + \beta e^{(-x/\gamma)} \tag{1}$$

where:

x = the distance to a point along the geogrid length (L), and
α, β, and γ = the parameters to be determined.

The values of x are normalized to the length of the geogrid specimen L. Thus, x ranges from 0 to 1, with $x = 0$ at the active end of the geogrid, and $x = 1$ at the passive end of the geogrid.

Equation 1 meets the boundary conditions of the pullout tests conducted in this study. Since the passive end of the geogrid ($x = 1.00$L) is free to move, the strain of the geogrid at $x = 1.00$L must be zero. Thus, the derivative of the equation at this value of x must be zero. Consequently, the plot of the equation needs to be horizontal or near horizontal at $x = 1.00$L.

Moreover, the equation needs to intersect the y-axis. This is because the strains at the active end of the geogrid should be smaller than the strains at the ultimate tensile strength of the material. Accordingly, equations with a power form ($y = \alpha x^{-\beta}$),

reciprocal form ($y = \alpha + \beta/x$) and logarithmic form ($y = \alpha + \beta \cdot \log(x)$) could not be adopted since the value of y at $x = 0$ tends to infinite in these equations.

Finally, the equation should allow determination of its derivative. Preference was given to equations that could be linearized in order to facilitate determination of the best fit using linear regression models. Inspection of Eq 1 reveals that the parameter α controls the distance of the curve from the x-axis, parameter β controls the inclination of the entire curve, and parameter γ controls the curvature of the curve.

The procedure followed to find the parameters to fit Eq 1 to the data shown in **Fig. 18** involved transforming the horizontal axis, so that Eq 1 becomes linear. The transformation of the horizontal axis is as follows:

(2)
$$x' = e^{(-x/\gamma)}$$

Thus, Eq 1 becomes:

(3)
$$y = \alpha + \beta x'$$

Accordingly, parameters α and β can be found using Eq 3 by fitting a straight line to the data plotted against the transformed horizontal axis x'. However, the parameter γ is inherent to x'. Consequently, the solution to find the values of α, β, and γ that provided the best fit is iterative. The best fit was evaluated using the method of the least squares. The following steps were adopted to find the best fit for parameters α, β, and γ:

1. Adopt initial values for α, β, and γ and plot y against x'.
2. Calculate $\Sigma(y_i - \hat{y}_i)^2$, where y_i is a data point and $\hat{y}_i$ is the predicted value for the data point.
3. Use the tool "solver" in Microsoft Excel to minimize $\Sigma(y_i - \hat{y}_i)^2$ by changing the values of α, β, and γ.
4. Plot a straight line to fit the data in the plot of y against x'.
5. Visually inspect whether the data falls into a straight line and check the value of the coefficient of determination, r^2.
6. Adopt values for α, β, and γ different than those used in step 1.
7. Repeat steps 2 to 5 and check whether the new solution by "solver" converges to the same values found in step 3.

Steps 6 and 7 are necessary because the "solver" tool in Excel is an algorithm that finds a local optimum for the problem being analyzed (Fylstra et al. 1998). Thus, it is necessary to use different starting values for α, β, and γ to verify whether the solution provided by "solver" converged to the most probable best solution (i.e., the global optimum). The solution can also be verified by comparing the values of α and β provided by "solver" to the coefficients m and n of a regression line $y = n + mx'$ for the data plotted in y versus x' space. If the best solution has been found, then the value of α provided by "solver" should be the same as n, and the value of β should be

FIG. 19 Example of solution obtained with the "solver" tool in Microsoft Excel when the least squares are found (α and β coincide with the coefficients of the regression line).
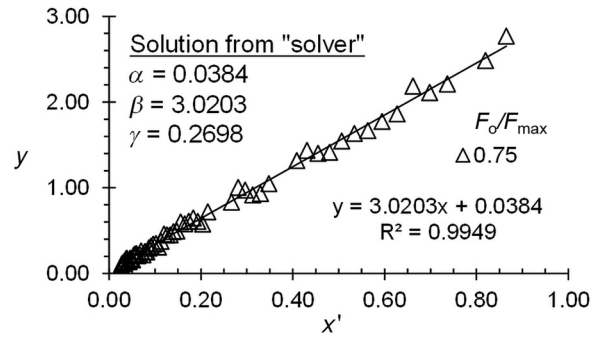
the same as m. This was the case when the best fit corresponded to positive values of α as shown in **Fig. 19**.

However, "solver" does not find the best solution for the least squares when the value of α for the best fit is negative. In this case, the value of α returned by "solver" is zero. Also, the values of α and β do not coincide with the values of n and m.

Figure 20 shows the curve fitted to the data from **Fig. 18** using the aforementioned procedure. The solid lines correspond to the curves fitted to data for different axial forces defined as a fraction of the maximum pullout force. The dashed lines show extrapolation of these curves to the intersection with the y-axis. Data points near the origin of the horizontal axis, which is the active end of the geogrid, influence significantly the parameter γ in Eq 1, which determines the curvature of the model fit. The value of the parameters used to fit the curves are listed in **Table 4**.

The residual plots of the fitted curves are shown in **Fig. 21**, where the residuals $y - \hat{y}i$ are plotted on the vertical axis against the predicted displacement, $\hat{y}i$, on the horizontal axis. **Figure 21** shows that the residuals increase with increasing displacements. Therefore, the data points near the active end of the geogrid,

FIG. 20 Exponential curves fitted to the data shown in **Fig. 18**: displacement profile of L3 at different load levels of the pullout test conducted with transparent soil and geogrid oriented in the MD confined under 35 kPa.
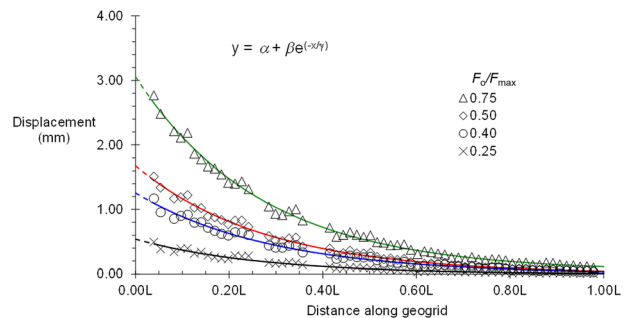
TABLE 4   Value of parameters used fit curves in **FIG. 20**.

$F_o/F_{\max}$	0.25	0.40	0.50	0.75
α	−0.0034	−0.0033	−0.0014	0.0384
β	0.5429	1.2605	1.6802	3.0203
γ	0.2658	0.2886	0.2761	0.2698

which are the ones with the largest displacements, dominate the curve fit.

CALCULATION OF GEOGRID STRAIN PROFILES

Strains along the geogrid can be calculated from the derivative of the functions defining the displacement data at the different fractions of the maximum pullout force. Thus:

(4) $$dy/dx = d\left(\alpha + \beta e^{(-x/\gamma)}\right)/dx = \beta d\left(e^{(-x/\gamma)}\right)/dx$$

Applying the chain rule to Eq 4 leads to the following solution:

(5) $$dy/dx = \beta e^{(-x/\gamma)}[d(-x/\gamma)/dx] = \beta e^{(-x/\gamma)}/\gamma$$

Thus, the derivative of Eq 1 is negative as shown in Eq 5. However, the geogrid deforms in tension in the pullout tests used in this study. Convention in engineering assigns a positive sign to tensile strains in geosynthetic materials. Consequently, the sign of Eq 5 was inverted to follow conventional practice. Accordingly, the tensile strain, ε, along the geogrid was calculated as follows:

(6) $$\varepsilon = \beta e^{(-x/\gamma)}/\gamma$$

Therefore, the strain profiles of the geogrid used in this study also follow an exponential equation, as shown in **Fig. 22**. It should be emphasized that while the adopted functions fitted well the response for the materials used in this study, additional research is needed to generalize this selection to other materials. The displacement and strain profiles may change for biaxial geogrids of similar geometry but composed of materials other

FIG. 21   Residuals plot of the fitted curves in **Fig. 20**.
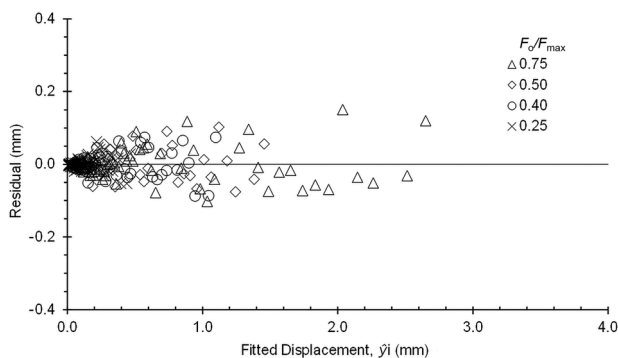
FIG. 22   Strain profile along the geogrid following an exponential curve, calculated from the curves fitted to the displacement data in **Fig. 20**.
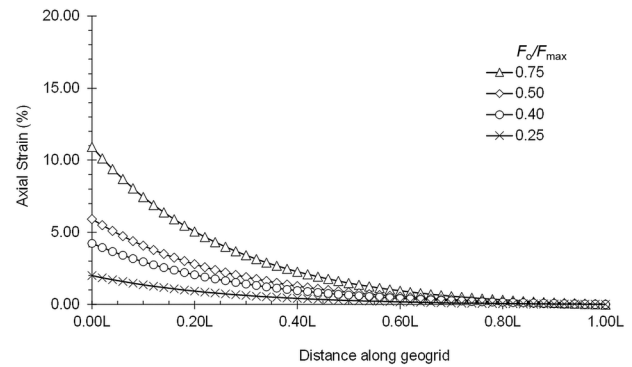
than polypropylene, or different junction strength and stiffness, or different shapes and stiffness of transverse ribs.

The shape of the strain profile of the geogrids calculated for the transparent pullout tests conducted in this research differs from the strain profiles reported by Chang et al. (1995) and Palmeira (2009). The exponential model used to describe the displacement profile data of the transparent pullout test showed in **Fig. 18** also seems able to describe the displacement profile data presented by Ezzein and Bathurst (2014) for confining pressures of 10 and 50 kPa, despite the significant differences in boundary conditions of the tests.

Ezzein and Bathurst (2014) tested geogrids with the passive end of the specimen (the one furthest away from the application of the pullout force) attached to a rear grip. Thus, strains are developed at the passive end of the geogrid when the entire specimen is mobilized in their tests. There are no strains developed at the passive end of the geogrid of the present study since our geogrid specimen was free to move.

On the other hand, when the geogrid specimen in the test setup from Ezzein and Bathurst (2014) is not fully mobilized, there is no strain developed at the end of the mobilized length. In this case, for all practical purposes, the test from Ezzein and Bathurst (2014) becomes with similar boundary conditions to the test of the present paper, in which no strains are developed at the passive end of the geogrid specimen. In this case, Eq 1 would apply to Ezzein and Bathurst's (2014) test with confining pressures of 10 and 50 kPa by considering the mobilized length as 1.00L.

This was not expected since the dimensions of the transparent pullout apparatus performed by Ezzein and Bathurst (2014) are several orders of magnitude larger than the dimensions of the apparatus used in the present study. On the other hand, the authors tested the same type of geogrid tested in the present study: an integrally formed polypropylene geogrid of the same model and manufacturer.

Chang et al. (1995) reported a linear distribution of strains along the geogrid. However, the strains were obtained using only 3 points along a high-density polyethylene (HDPE) uniaxial geogrid specimen. The strain distribution along geogrids reported by Palmeira (2009) is comparable to the strain distribution calculated in this paper. This occurred in spite of the significantly different dimensions between the setup of the test from Palmeira (2009) and the transparent pullout tests in the present research. The pullout test reported by Palmeira (2009) was conducted in a 1 m^3 pullout box with dimensions comparable to those recommended by the ASTM D6706 for traditional, large pullout tests, and a HDPE uniaxial geogrid specimen that was 600 mm long embedded in dense sand.

Thus, the similarity of the strain profile calculated in the present study to the strain profile reported by Palmeira (2009) adds evidence to the suitability of extrapolating the results from tests conducting using transparent soil to tests with natural soils. Also, similarity of the displacement profiles reported by Ezzein and Bathurst (2014) and by the present study is significant in spite of the differences in pullout box dimensions and testing boundary conditions.

Mobilization of Transverse Ribs

The transparent pullout test setup presented in this paper permits obtaining displacement data along transverse ribs during testing. These novel data are presented in **Fig. 23**, where the displacement profiles of the first five transverse ribs between L3 and L4, and closest to the front wall (at 0.08L, 0.20L, 0.33L, 0.44L, and 0.57L) are shown. The displacement profile of this segment of the transverse rib was normalized to its aperture width W, which corresponds to the distance between the two central longitudinal ribs L3 and L4 (equal to 36.6 mm). Thus $W = 0$ at the left end of the central segment of the transverse rib (junction with L3), and $W = 1$ at the other end (junction with L4).

In this test, the ratio of the spacing between successive transverse ribs (S) to the D_{50} of the transparent soil is 5.5. Higher scatter is observed on the displacement data from the transverse rib at 0.08L (**Fig. 23(a)**) in relation to the other transverse ribs because this is the transverse rib subjected to the largest displacements. Thus, this rib is more susceptible to scratching and unbinding of the white dots on the rib due to friction against the sharp edges of the adjacent fused quartz particles.

FIG. 23

Displacement profiles of transverse ribs between L3 and L4 of the geogrid during pullout testing oriented in the MD, embedded in transparent soil under a confinement of 35 kPa: (a) rib at 0.08L, (b) rib at 0.20L, (c) rib at 0.33L, (d) rib at 0.44L and (e) rib at 0.57L. Note: 1.00 W is the aperture size between longitudinal ribs L3 and L4.
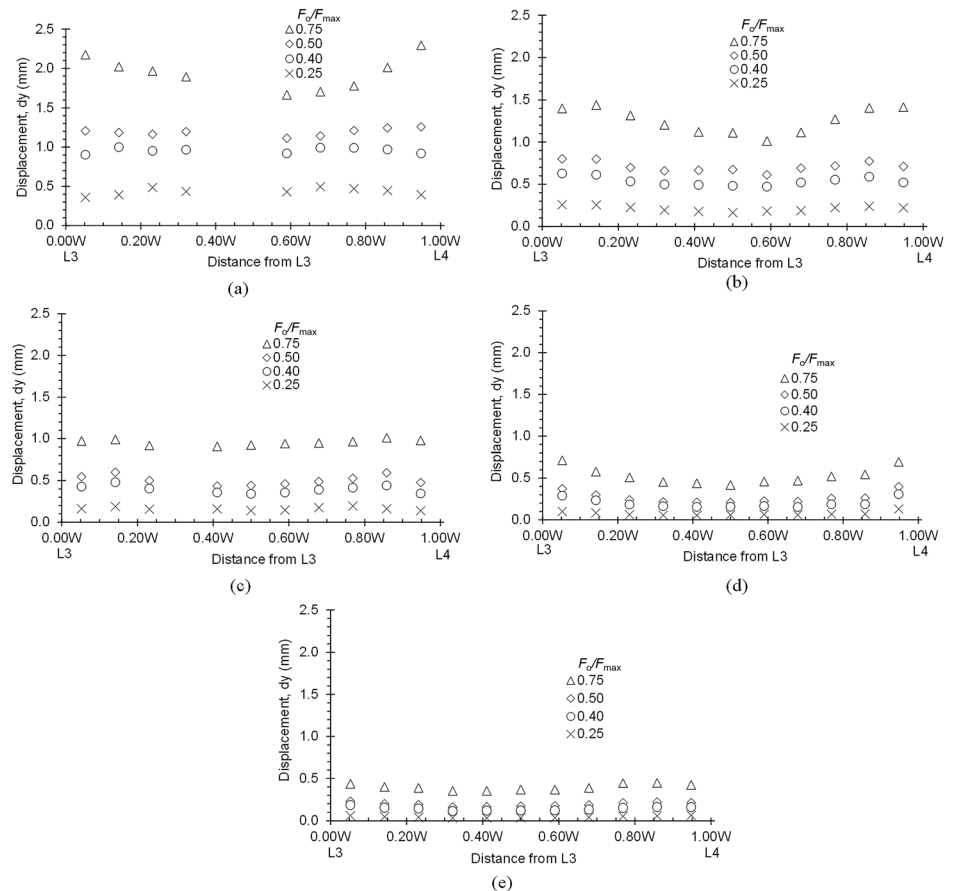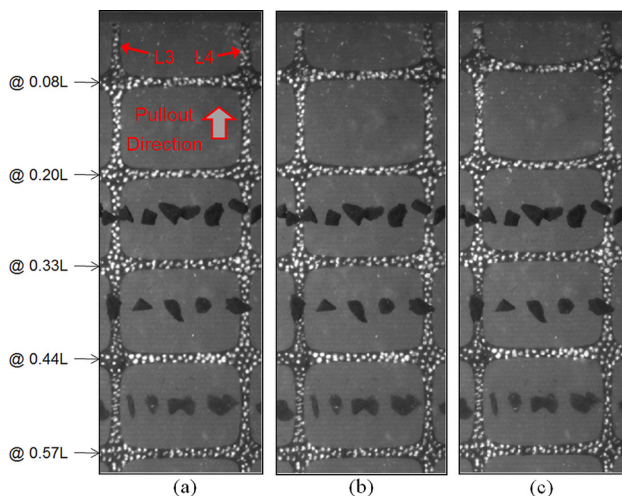
Figure 24 shows a close view of the transverse ribs whose displacement profile data are presented in Fig. 23 at different stages of the pullout tests corresponding to axial force values of 0.00, 0.75, and 1.00 F_o/F_{max}. The progressive mobilization of the transverse ribs can be observed in the figure. The transverse ribs are in their original shape at the beginning of the test (**Fig. 24(*a*)**). Then, visual deflections of the top two transverse ribs can be observed at an intermediate state of the test (**Fig. 24(*b*)**). Finally, significant deflections, especially of the top rib, are observed at the end of the test when the ultimate pullout force was reached (**Fig. 24(*c*)**).

Figure 23 shows that at 0.75 F_o/F_{max}, the transverse rib at 0.08L (**Fig. 23(*a*)**) deflects more than the transverse rib at 0.20L (**Fig. 23(*b*)**); which in turn deflects more than the transverse rib at 0.33L (**Fig. 23(*c*)**). However, despite its larger displacements, the transverse rib at 0.33L deflects less than the transverse rib at 0.44L (**Fig. 23(*d*)**). Subsequently, the initial pattern of smaller deflections in ribs further along the geogrid is observed again, with the transverse rib at 0.44L (**Fig. 23(*d*)**) deflecting more than the rib at 0.57L (**Fig. 23(*e*)**).

The observed behavior of the transverse ribs is different from the results obtained by the soil–geogrid interaction model developed by Palmeira (2004). Specifically, Palmeira (2004) reported that the second transverse rib closest to the front wall was the one that underwent the greatest mobilization of the bearing mechanism. The author indicated that the images from the photo-elasticity study by Dyer (1985) from a test with multiple transverse ribs suggest similar behavior of the transverse ribs. The significant advantage of the transparent pullout testing setup presented in this paper is that the progressive mobilization of the transverse ribs can be accurately evaluated.

In particular, the results from Fig. 23 exemplify the complexity involving soil–geogrid interaction and the interference between transverse ribs. The data show that there is high interference between transverse ribs, and that the pattern of interference is complex. For example, it was expected that the transverse ribs that are more distant from the active end of the geogrid would show smaller deflections.

In addition, the results suggest that, for the relatively closely spaced transverse ribs ($S/D_{50} = 5.5$) of the geogrid used in this test, the size of the disturbed zone behind the ribs decreased with increasing distance from the active end of the geogrid (in this case, ribs located from 0.08L to 0.33L). Then, after a certain point, this zone behind a transverse rib appears to become less disturbed, so that the next transverse rib was more engaged (transverse rib at 0.44L). After that, this transverse rib that was more engaged than the previous one, leaving behind a disturbed zone of soil that prevented the next transverse rib (rib at 0.57L) to fully develop its bearing stress capacity.

Finally, deflection of the transverse ribs were first measured at early stages of the test, when only 25 % of the maximum pullout force had developed. For example, Fig. 23(*b*) shows a central deflection of the transverse rib at 0.20L of 0.095 mm at 0.25 F_o/F_{max}. The deflection of the transverse suggest its engagement and development of the bearing mechanism.

In addition, the results from small transparent pullout tests using geogrids from the same roll of the geogrid used in the present study but without transverse ribs and with one transverse rib showed significant differences in generated pullout forces at early stages of the test (Ferreira and Zornberg 2014). This difference was observed with a displacement of only 0.20 mm of a reference point at the mid-length of the geogrid, which corresponds to approximately 0.25 F_o/F_{max} of the test with one transverse rib. Significant deflections of the transverse rib were also measured at this stress level.

These findings contradict the observations made by Farrag et al. (1993) and Teixeira et al. (2007), who concluded that the bearing mechanism was mobilized only at relatively late stages of the tests. However, their tests were conducted with geogrids different than the one used in the present paper. Different results may be obtained for the mobilization of the bearing mechanism and interference between transverse ribs with other geogrid products. The behavior of transverse ribs is expected to depend not only on the distance between them, but also on their stiffness and the stiffness of their junctions (Palmeira 2009).

Displacement of Soil Markers

Particles of crushed fused quartz were spray-painted in black and used as soil markers within the mass of transparent soil compacted in the pullout box. These soil markers were placed between compaction lifts. The soil markers were placed along lines that were perpendicular (plan view in **Fig. 4(*b*)**) and

FIG. 25   Position of soil markers with the distances from the interface soil–geogrid (i.e., geogrid plane).
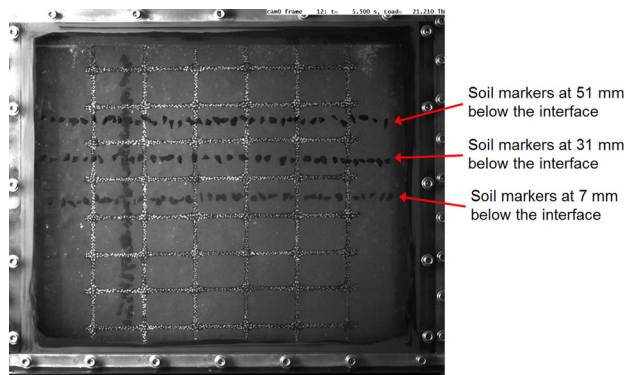
parallel to the direction of pullout (side view in **Fig. 4(c)**), thus allowing 3D visualization of soil–geogrid interaction during testing.

However, tracking of the soil markers with ACC and DIC were affected by the contrast created by the black fused quartz particles in the transparent medium, which was not as significant as the contrast created with white dots painted on the black geogrid. Movement of the pullout box was noticeable towards the end of the tests above 80 % of the developed maximum pullout force. The movement of the box was not continuous and occurred in incremental steps.

The displacement of the box was measured by tracking movement of the screws of the box, which provided satisfactory contrast, and thus DIC could be used to calculate the displacements. The movement of the box affected measurements on the side view, since box displacements were in the same order of magnitude of the displacements of the soil markers in the transparent soil mass. Yet, measurements along the geogrid were not affected because displacements along the geogrid were two orders of magnitude larger than the movement of the box in the plan view. Accordingly, the displacements of the soil markers only in the plan view (**Fig. 4(b)**) are qualitatively analyzed in this paper.

The lines of soil markers placed perpendicular to the pullout direction and observed in the plan view were at distances of 51, 31, and 7 mm from the interface (**Fig. 25**). These distances correspond, respectively, to the lines of markers in the top, middle and bottom shown in **Fig. 25**. No displacements were observed for the soil markers at distances of 51 and 31 mm from the interface throughout the test. No displacements were determined for the soil markers closest to the interface (bottom line in **Fig. 25**) until 0.75 F_o/F_{max}. Then, relatively small displacements of these markers were observed between 0.75 and 1.00 F_o/F_{max}.

Thus, it can be concluded that for the transparent soil and polypropylene geogrid used in this research, the observed boundary of the zone of influence of the geogrid ranged between 7 and 31 mm from the interface. This is equivalent to between 2 and 8 times the D_{50} of the soil. The ratio between the D_{50} of the soil and the thickness of the transverse ribs is 4.4.

Summary and Conclusions

This paper presented a new, 3D small transparent pullout test setup developed to study the mechanisms of soil–geogrid interaction. The test setup involves a pullout box with transparent bottom plate and sidewalls that permit visualization of the soil–geogrid interface on the plan and side views when testing with transparent soil. The test setup also involves a transparent soil composed of crushed fused quartz and a mineral oil mix, an image acquisition system with two high-resolution CCD cameras controlled by LabView.

Displacement data along the geogrid specimen and of soil markers at different distances from the interface were obtained using digital image correlations through ACC and DIC technology. Validation of the DIC calculations with DynamicStudio v.2.30, a commercial program, was performed with data from ultimate tensile strength tests of the polypropylene geogrid used in this study. These tests were conducted with the developed image acquisition system and calculations performed with the DIC program. The results were compared to the results of the tests conducted by Gupta (2009) with geogrid specimens from the same lot at a commercial laboratory. Good agreement was found between the results.

A series of direct shear and small pullout tests were conducted to compare the results of the tests with fused quartz to the results of tests with Monterey #30 sand. The results showed that the transparent soil of this study can be used as a surrogate for sands, with the general shape of the pullout curves in agreement with pullout test data reported in the literature.

A small transparent pullout test was conducted with a confining pressure of 35 kPa, and displacement profiles of the geogrid and its transverse ribs were obtained with continuous data from a dense distribution of measurement points. It was concluded that displacements along the polypropylene geogrid used in this study can be well represented by an exponential function of the form of $y = \alpha + \beta e^{(-x/\gamma)}$; where x is the distance along the geogrid, and α, β, and γ are experimental parameters obtained through data fitting.

Strain profiles along the geogrid were derived from the function used to describe the displacement profiles along the geogrid. The strain profiles found are also in the form of an exponential function but following the slightly different equation $[\beta e^{(-x/\gamma)}]/\gamma$.

Novel data and images were obtained showing the local deflections of transverse ribs at different distances from the front wall. A complex progressive mobilization of the transverse ribs was observed. The data showed that the expected decreasing trend of deflections in transverse ribs with increasing

distance from the front wall, the smaller the deflection of the rib, was not valid for the test performed. In fact, the results suggested that the zone of disturbance behind transverse ribs varied in size in a nonlinear pattern. Additionally, deflections of transverse ribs were measured at comparatively early stages of the test, when only 25 % of the maximum pullout force had developed.

Finally, qualitative analysis from the plan view images of the displacement of soil markers was performed. It was concluded that the observed boundary of the zone of influence of the geogrid and transparent soil tested ranges between 7 and 31 mm from the interface, which corresponds to 2 to 8 times the D_{50} of the soil.

References

Allen, T. M., Bathurst, R. J., Holtz, R. D., Walters, D., and Lee, W. F., 2003, "A New Working Stress Method for Prediction of Reinforcement Loads in Geosynthetic Walls," *Can. Geotech. J.*, Vol. 40, No. 5, pp. 976–994.

ASTM D3080/D3080M-11, 2011: Standard Test Method for Direct Shear Test of Soils Under Consolidated Drained Conditions, ASTM International, West Conshohocken, PA, www.astm.org.

ASTM D4595-11, 2011: Standard Test Method for Tensile Properties of Geotextiles by the Wide-Width Strip Method, ASTM International, West Conshohocken, PA, www.astm.org.

ASTM D6637-11, 2011: Standard Test Method for Determining Tensile Properties of Geogrids by the Single or Multi-Rib Tensile Method, ASTM International, West Conshohocken, PA, www.astm.org.

ASTM D6706-01(2013), 2013: Standard Test Method for Measuring Geosynthetic Pullout Resistance in Soil, ASTM International, West Conshohocken, PA, www.astm.org.

Bathurst, R. J., Miyata, Y., Nernheim, A., and Allen, A. M., 2008, "Refinement of K-Stiffness Method for Geosynthetic-Reinforced Soil Walls," *Geosynth. Int.*, Vol. 15, No. 4, pp. 269–295.

Berg, R. R., Christopher, B. R., and Perkins, S., 2000, "Geosynthetic Reinforcement of the Aggregate Base/Subbase Courses of Pavement Structures," *GMA White Paper II,* Geosynthetic Materials Association, Roseville, MN.

Berg, R. R., Christopher, B. R., and Samtani, N. C., 2009, "Design of Mechanically Stabilized Earth Walls and

Reinforced Soil Slopes—Volume I," *FHWA-NHI-10-024 Report*, Federal Highway Administration, Washington, D.C.

Chang, D. T., Sun, T. S., and Hung, F. Y., 1995, "Pullout Mechanism of Geogrids Under Confinement by Sandy and Clayey Soils," *Transp. Res. Rec.*, Vol. 1474, pp. 64–72.

Cuelho, E., Perkins, S., and Morris, Z., 2014, "Relative Operational Performance of Geosynthetics Used As Subgrade Stabilization," *Report FHWA/MT-14-002/7712-251*, Federal Highway Administration, Washington, D.C.

Dantec Dynamics, 2005, *2D PIV Reference Manual*, Dantec Dynamics, Tonsbakken, Denmark.

Dias, A. C., 2003, "Numerical Analyses of Soil–Geosynthetic Interaction in Pull-Out Tests," MS.c. thesis, University of Brasilia, Brasilia, Brazil (in Portuguese).

Dyer, M. R., 1985, "Observations of the Stress Distribution in Crushed Glass With Applications to Soil Reinforcement," Ph.D. thesis, University of Oxford, Oxford, UK.

Ezzein, F. M. and Bathurst, R., 2011a, "A Transparent Sand for Geotechnical Laboratory Modeling," *Geotech. Test. J.*, Vol. 34, No. 6, pp. 1–12.

Ezzein, F. M. and Bathurst, R., 2011b, "Development of a Geosynthetic Pullout Test Apparatus With Transparent Granular Soil," presented at the *2011 Joint Pan-American Canadian Geotechnical Society Geotechnical Conference*, Toronto, ON, Oct 2–6, ISSMGE, Richmond, BC, -unpublished. Available at http://geoserver.ing.puc.cl/info/conferences/PanAm2011/panam2011/pdfs/GEO11Paper688.pdf

Ezzein, F. M. and Bathurst, R., 2014, "A New Approach to Evaluate Soil–Geosynthetic Interaction Using a Novel Pullout Test Apparatus and Transparent Granular Soil," *Geotext. Geomembr.*, Vol. 42, No. 3, pp. 246–255.

Farrag, K., Acar, Y. B., and Juran, I., 1993, "Pull-Out Resistance of Geogrid Reinforcements," *Geotext. Geomembr.*, Vol. 12, No. 2, pp. 133–159.

Ferreira, J. A. Z. and Zornberg, J. G., 2014, "Behavior of Transverse Ribs in a Tensioned Geogrid Embedded in Transparent Soil," presented at the *10th ICG—International Conference on Geosynthetics*, Berlin, Germany, Sept 21–25, German Geotechnical Society, Essen, Germany, -unpublished. Available at http://www.10icg-berlin.com/en/proceedings.html

Fylstra, D., Lasdon, L., Watson, J., and Waren, A., 1998, "Design and Use of the Microsoft Excel Solver," *Interfaces*, Vol. 28, No. 5, pp. 29–55.

Gill, D. R. and Lehane, B. M., 2001, "An Optical Technique for Investigating Soil Displacement Patterns," *Geotech. Test. J.*, Vol. 24, No. 3, pp. 324–329.

Gupta, R., 2009, "A Study of Geosynthetic Reinforced Flexible Pavement System," Ph.D. thesis, The University of Texas at Austin, Austin, TX.

Jensen, K. D., 2004, "Flow Measurements," *Proceedings of ENCIT 2004: 10th Brazilian Conference of Thermal Engineering and Sciences*, Rio de Janeiro, Brazil, Nov 29–Dec 3, Taylor and Francis, London, pp. 1–24.

Jewell, R. A., 1992, "Strength and Deformation on Reinforced Soil Design," *Proceedings of the Fourth International Conference on Geotextiles, Geomembranes and Related Products*, Vol. 3, The Hague, The Netherlands, May 28–June 1, Balkema, Rotterdam, The Netherlands, pp. 913–946.

Jewel, R. A., Milligan, G. W. E., Sarsby, R. W., and DuBois, D., 1984, "Interaction Between Soil and Grids," *Proceedings of

the *Symposium on Polymer Grid Reinforcement in Civil Engineering*, London, UK, March 22–23, Thomas Telford, London, pp. 18–30.

Keane, R. D. and Adrian, R. J., 1992, "Theory of Cross-Correlation Analysis of PIV Images," *Appl. Sci. Res.*, Vol. 49, No. 3, pp. 191–215.

Li, C., 2005, "Mechanical Response of Fiber-Reinforced Soil," Ph.D. thesis, The University of Texas at Austin, Austin, TX.

Liu, J. and Iskander, M., 2004, "Adaptive Cross Correlation for Imaging Displacements in Soils," *J. Comput. Civ. Eng.*, Vol. 18, No. 1, pp. 46–57.

McKelvey, D., Sivakumar, V., Bell, A., and Graham, J., 2004, "Modeling Vibrated Stone Columns in Soft Clay," *Proc. Inst. Civ. Eng.*, Vol. 157, No. GE3, pp. 137–149.

Nakamura, T., Mitachi, T., and Ikeura, I., 2003, "Estimating Method for the In–Soil Deformation Behavior of Geogrid Based on the Results of Direct Box Shear Test," *Soil Found.*, Vol. 43, No. 1, pp. 47–57.

Ochiai, H., Otani, J., Hayashic, S., and Hirai, T., 1996, "The Pullout Resistance of Geogrids in Reinforced Soil," *Geotext. Geomembr.*, Vol. 14, No. 1, pp. 19–42.

Palmeira, E. M., 2004, "Bearing Force Mobilization in Pullout Tests on Geogrids," *Geotext. Geomembr.*, Vol. 22, No. 6, pp. 481–509.

Palmeira, E. M., 2009, "Soil–Geosynthetic Interaction: Modelling and Analysis," *Geotext. Geomembr.*, Vol. 27, No. 5, pp. 368–390.

Palmeira, E. M. and Milligan, W. E., 1989, "Scale and Other Factors Affecting the Results of Pull-Out Tests of Grids Buried in Sand," *Geotechnique*, Vol. 39, No. 3, pp. 511–524.

Perkins, S. W. and Ismeik, M., 1997, "A Synthesis and Evaluation of Geosynthetic-Reinforced Base Layers in Flexible Pavements: Part I," *Geosynth. Int.*, Vol. 4, No. 6, pp. 549–604.

Raffel, M., Willert, C. E., Wereley, S. T., and Kompenhans, J., 2007, *Particle Image Velocimetry: A Practical Guide*, Springer, New York.

Ren, H. and Wu, S. T., 2012, *Introduction to Adaptive Lenses*, Wiley, New York.

Sadek, S., Iskander, M., and Liu, J., 2002, "Geotechnical Properties of Transparent Silica," *Can. Geotech. J.*, Vol. 39, No. 1, pp. 111–124.

Song, Z., Hu, Y., O'Loughlin, C., and Randolph, M. F., 2009, "Loss in Anchor Embedment During Plate Anchor Keying in Clay," *J. Geotech. Geoenviron. Eng.*, Vol. 135, No. 10, pp. 1475–1485.

Teixeira, S. H. C., Bueno, B. S., and Zornberg, J. G., 2007, "Pullout Resistance of Individual Longitudinal and Transverse Geogrid Ribs," *J. Geotech. Geoenviron. Eng.*, Vol. 133, No. 1, pp. 37–50.

Wakabayashi, T., 1950, "Photo-Elastic Method for Determination of Stress in Powdered Mass," *J. Phys. Soc. Jpn.*, Vol. 5, No. 5, pp. 383–385.

Wei, J., Chua, K. C., Lim, S. K., Chew, S. H., Karunaratner, S. A., and Seah, Y. T., 2002, "Performance of a Geosynthetic Reinforced Steep Slope in Residual Soil," *Proceedings of the 7th International Conference on Geosynthetics (ICG)*, Nice, France, Sept 22–27, Balkema, Rotterdam, The Netherlands, pp. 325–328.

White, D. J., Take, W. A., and Bolton, M. D., 2003, "Soil Deformation Measurement Using Particle Image Velocimetry (PIV) and Photogrammetry," *Geotechnique*, Vol. 53, No. 7, pp. 619–632.

Zornberg, J. G., Barrows, R. J., Christopher, B. R., and Wayne, M. H., 1995, "Construction and Instrumentation of a Highway Slope Reinforced With High-Strength Geotextiles," *Proceedings of Geosynthetics'95*, Nashville, TN, Vol. 1, Feb 21–23, Industrial Fabric Association International, Roseville, MN, pp. 13–28.

Zornberg, J. G., Ferreira, J. A. Z., and Roodi, G. H., 2013, "Geosynthetic-Reinforced Unbound Base Courses: Quantification of the Reinforcement Benefits," *CTR Report No. FHWA/TX-12/5-4829-01-2*, Center for Transportation Research, Austin, TX.